

# Fluid-particle heat transfer in static assemblies: Effect of particle shape



Qi Chang <sup>a,b</sup>, Liqiu Yang <sup>b,c</sup>, Wei Ge <sup>b,c,d,\*</sup>

<sup>a</sup> School of Chemical Engineering and Technology, Tianjin University, Tianjin 300072, China

<sup>b</sup> State Key Laboratory of Multiphase Complex Systems, Institute of Process Engineering, Chinese Academy of Sciences, Beijing 100190, China

<sup>c</sup> School of Chemical Engineering, University of Chinese Academy of Sciences, Beijing 100049, China

<sup>d</sup> Innovation Academy for Green Manufacture, Chinese Academy of Sciences, Beijing 100190, China

## ARTICLE INFO

### Article history:

Received 5 April 2020

Revised 10 November 2020

Accepted 15 November 2020

Available online 15 December 2020

### Keywords:

heat transfer

static assemblies

spheroid

sphere

oblate

prolate

## ABSTRACT

The heat transfer in fluid flow through static assemblies of randomly distributed spheroids, including spheres, prolates, and oblates, is investigated using direct numerical simulation (DNS). Constant heat fluxes are imposed at individual particle surface by the Neumann boundary condition for temperature. The superficial Reynolds number ( $Re$ ) and the solid volume fraction ( $\varphi$ ) range from 2.5 to 200, and from 0.1 to 0.3, respectively. The simulation results for spheres and prolates agree well with the DNS data and correlations in literature and new correlations for prolates and oblates are proposed. With these results, the particle shape effect on the average Nusselt number ( $Nu_{avg}$ ) is described more comprehensively: At low  $\varphi$  (e.g., 0.1), the  $Nu_{avg}$  for prolates and oblates are higher than that of spheres, and as  $Re$  increases, the  $Nu_{avg}$  of oblates gradually catches up that of prolates and becomes comparable at  $Re \approx 200$ . Moreover, oblates attenuate and intensify the heat transfer at low and high  $Re$  at high  $\varphi$ , respectively.

© 2020 Published by Elsevier Ltd.

## 1. Introduction

Fluid-particle systems present in many processes in chemical industries. As for interphase momentum transfer, an in-depth understanding of the interphase heat transfer at particle-resolved scale is important for the modeling, designing, and scaling-up of the equipment and processes involving these systems. In general, the interphase heat transfer rate is characterized by the Nusselt number,

$$Nu = h d_e / k \quad (1)$$

with  $h$ ,  $d_e$ , and  $k$  being the heat transfer coefficient (which is scale and location dependent with its exact meaning specified by the problem studied), the equivalent sphere diameter and the fluid heat conduction coefficient, respectively.

$$d_e = (6V_p/\pi)^{1/3} \quad (2)$$

with  $V_p$  the particle volume. Therefore,  $h$ , and thus  $Nu$ , are usually functions of the superficial Reynolds number  $Re$ , the solid volume fraction  $\varphi$ , the particle geometric parameter (which accounts for the effect of particle shape and orientation) and the thermal prop-

erties, e.g., the Prandtl number  $Pr=c_p\mu/k$  with  $c_p$  the fluid specific heat capacity and  $\mu$  the fluid viscosity.

However, even for spheres, no general and accurate correlation of  $Nu$  is well-accepted for the diverse conditions encountered in engineering practice. Experimentally, the dataset so far scatters over several orders of magnitude of  $Re$ , with wide intervals of no data [1], as it is difficult to study different factors independently. For example, in fluidized bed,  $Re$  and  $\varphi$  are inter-dependent and it is difficult to get the  $Nu$  at a given  $Re$  for different  $\varphi$ , and vice versa. Experimental measurements also lack the details of the flow and temperature field that can reveal the mechanism of heat transfer to guide the development of sophisticated correlations of  $Nu$ . Numerical simulation may complement the limitations of experimental methods to study the heat transfer in more details, among which direct numerical simulation (DNS) may reach an accuracy, at the macro-scale, comparable to experimental measurements, and is hence receiving more and more attention. For example, several correlations for  $Nu$  of spheres from low to moderate  $Re$  up to 200 and solid volume fractions up to 0.5 have been obtained so far [2–7] and extended to bi-disperse systems recently [8,9].

As summarized in Table 1, most DNS studies on non-spherical particles focus on axisymmetric ellipsoids, namely spheroids. In Fig. 1, they are classified into oblates ( $c < a$ ), spheres ( $c = a$ ) and prolates ( $c > a$ ), with  $c$  and  $a$  being the semi-axis lengths in the axisymmetric (or polar symmetric) direction and the other two direc-

\* Corresponding author.

E-mail address: [wge@ipe.ac.cn](mailto:wge@ipe.ac.cn) (W. Ge).

**Table 1**  
DNS studies on the heat transfer between fluids and spheroids.

Reference	$\varphi$	$Re$	$AR$	System
He et al. [7]	0.1–0.35	10–200	2.5	Assembly assembly
Ke et al. [13]	-	10–200	0.25–2.5	Isolated
Richter & Nikrityuk [14,15]	-	10–250	2.0	Isolated

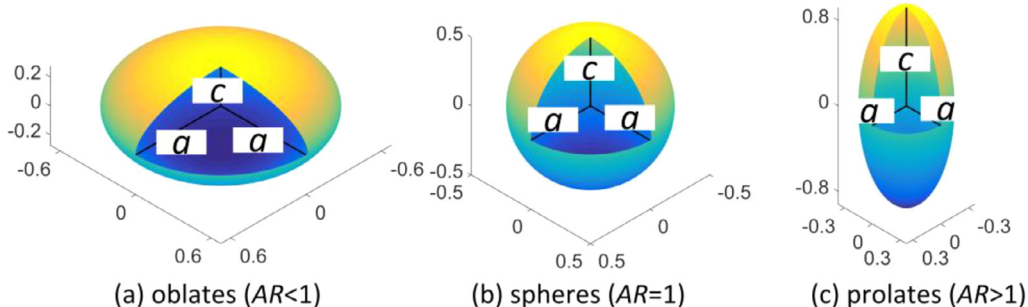


Fig. 1. Schematics of different spheroids characterized by  $AR$ .

tions (or equatorial plane), respectively. For heat transfer in static particle assemblies [7], oblates were not included yet, however, as known for the drag coefficient [10], the interphase transport properties of spheroid assemblies may depend significantly on their aspect ratio,  $AR=c/a$ . In fact, Gan et al. [11] demonstrated that  $AR$  affects the thermal behavior significantly in fluid-particle systems by coupling computational fluid dynamics (CFD) and discrete element method (DEM). However, the used  $Nu$  correlations had been developed in systems with isolate 2D particles [12] without considering the effects of  $\varphi$  and realistic 3D particles. This work, therefore, extends the DNS studies to oblates to understand the effect of  $AR$  more comprehensively.

## 2. Numerical methods

Though conventional body-fitted methods, e.g., [16], are available for the DNS of fluid flow in static particle assemblies, an in-house code, employing the immersed boundary method (IBM) to describe the solid-fluid coupling, was used in this work considering its computational efficiency and potential to simulate free-moving particles [17,18]. The IBM makes use of two different grids: a fixed Cartesian grid (Eulerian) for the fluid and a grid attached to the particle surface (Lagrangian). The numerical methods are outlined below.

### 2.1. Governing equations

The mass and momentum conservation is described by the Navier-Stokes equations for unsteady, incompressible, Newtonian fluid flow, that is:

$$\nabla \cdot \mathbf{u} = 0 \quad (3)$$

$$\rho(\partial \mathbf{u}/\partial t + \mathbf{u} \cdot \nabla \mathbf{u}) = \nabla \cdot \boldsymbol{\tau} + \mathbf{f} \quad (4)$$

where  $t$  is time, and the stress tensor  $\boldsymbol{\tau} = -p\mathbf{I} + \mu[(\nabla \mathbf{u}) + (\nabla \mathbf{u})^T]$  with  $p$  and  $\mathbf{u}$  the local pressure and velocity of the fluid and  $\mathbf{f}$  the body force imposing the no-slip boundary condition at particle surface (described in Section 2.2.1), respectively. The energy conservation equation is, correspondingly,

$$\rho c_p(\partial T/\partial t + \mathbf{u} \cdot \nabla T) = k\nabla^2 T \quad (5)$$

where  $T$  is the local fluid temperature.

### 2.2. Fluid-particle coupling

In this work, the core issue of the fluid-particle coupling is the proper enforcement of the boundary conditions of velocity and temperature at particle surface. In IBM, they may follow a number of schemes [19]. In this study, to satisfy the no-slip boundary condition at particle surface and to keep constant normal temperature gradient there in some cases (as explained later), the Dirac delta function (DDF) direct forcing method [20] for the  $\mathbf{u}$  in Eq. (4) and the ghost-cell (GC) method [21] for the  $T$  in Eq. (5) were employed, respectively.

#### 2.2.1. The DDF-IBM

The DDF-IBM imposing Dirichlet boundary conditions for velocity has been documented in [20,22,23]. Its numerical treatment is briefly presented below. It introduces the  $\mathbf{f}$  in Eq. (4) to impose the no-slip boundary condition in the immediate vicinity of particle surface. Interpolation and spreading are needed to communicate the quantities on the two grids based on the regularized DDF [24] with a width of three Eulerian grid cells:

$$\delta^{(3)}(\mathbf{x}_{i,j,k} - \mathbf{X}_L) = \delta^{(1)}(x_{i,j,k} - X_L)\delta^{(1)}(y_{i,j,k} - Y_L)\delta^{(1)}(z_{i,j,k} - Z_L) \quad (6a)$$

Taking the  $x$ -component as an instance,

$$\delta^{(1)}(x_{i,j,k} - X_L) = \psi[(x_{i,j,k} - X_L)/\Delta x] \quad (6b)$$

where  $\psi$  is given by,

$$\psi(r) = \begin{cases} 1/6(5 - 3|r| - \sqrt{-3(1 - |r|)^2 + 1}), & 0.5 \leq |r| \leq 1.5 \\ 1/3(1 + \sqrt{-3r^2 + 1}), & |r| \leq 0.5 \\ 0, & \text{otherwise.} \end{cases} \quad (6c)$$

For the computation of the body force  $\mathbf{f}$  in Eq. (4),  $\mathbf{u}_{i,j,k}$  on the Eulerian grid is first interpolated to  $\mathbf{U}_L$  at the  $L$ th Lagrangian point  $\mathbf{X}_L$ :

$$\mathbf{U}_L = \sum_{i,j,k} \mathbf{u}_{i,j,k} \delta^{(3)}(\mathbf{x}_{i,j,k} - \mathbf{X}_L) \quad (7a)$$

Then the force  $\mathbf{F}_L$  at  $\mathbf{X}_L$  is calculated by

$$\mathbf{F}_L = (\mathbf{U}_p - \mathbf{U}_L)/\Delta t \quad (7b)$$

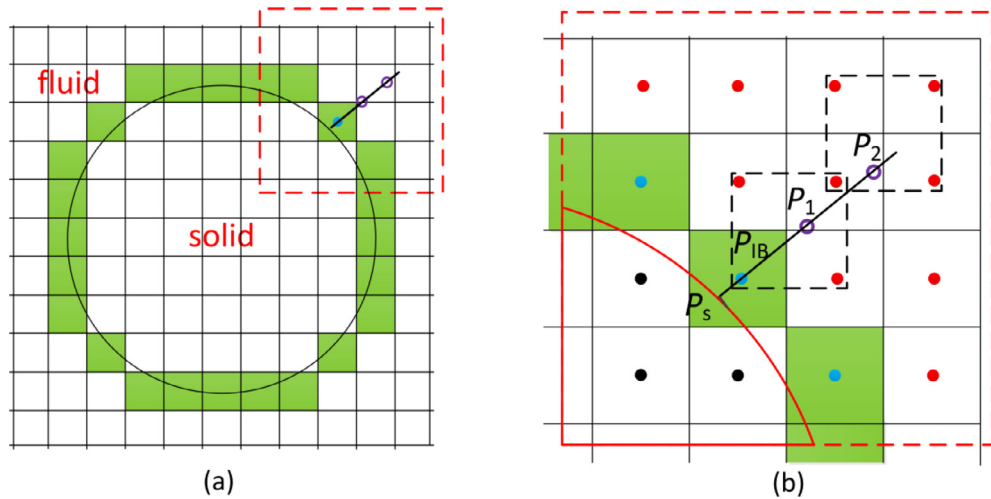


**Fig. 2.** Schematics of the flag identification and interpolation of temperature in a typical IB cell. (The solid surface is represented by a circle in 2D, this numerical approach was actually used for all spheroids in this work, including spheres, prolates, and oblates in 3D.)

and finally  $\mathbf{F}_L$  is spreaded to  $\mathbf{f}_{i,j,k}$  on the Eulerian grid:

$$\mathbf{f}_{i,j,k} = \sum_L \mathbf{F}_L \delta^{(3)}(\mathbf{x}_{i,j,k} - \mathbf{X}_L) \Delta V_L / \Delta x \Delta y \Delta z \quad (7c)$$

where the subscripts  $i, j, k$  are the cell indexes on the Eulerian grid.  $\mathbf{U}_p$  is the desired solid velocity (actually being zero in this work, as the particles are static and no-slip boundary condition is applied at the particle surface) and  $\mathbf{U}_L$  is the interpolated fluid velocity at the  $L$ th Lagrangian point. In principle, the interphase force  $\mathbf{F}_p$  on a particle can be calculated from the derivative of the velocity and pressure fields near the particle surface and then integrated over the particle. For the DDF-IBM, however, the fields are contaminated due to surface smearing there. Thus, for higher accuracy in closed domains (e.g., particles),  $\mathbf{F}_p$  is calculated [20,22,23,25,26] as

$$\mathbf{F}_p = \oint_{S_p} \boldsymbol{\tau} \cdot \mathbf{n} dS_p \approx d/dt \int_{V_p} \rho \mathbf{u} \Delta x \Delta y \Delta z - \sum_{L=1:N_L} \rho \mathbf{F}_L \Delta V_L \quad (8a)$$

In particular, when the particles are static,  $d/dt \int_{V_p} \rho \mathbf{u} \Delta x \Delta y \Delta z = 0$ , thus Eq. (8a) can be simplified to

$$\mathbf{F}_p = - \sum_{L=1:N_L} \rho \mathbf{F}_L \Delta V_L \quad (8b)$$

### 2.2.2. The GC-IBM

The GC-IBM has been well documented in [7,21,27], but for the sake of completeness, its numerical treatment is briefly presented and extended to spheroidal particles based on a simple point-surface distance computation method [28]. The whole procedure can be divided into 4 parts: flag assignment; calculation of the surface point ( $\mathbf{P}_s$ ) with the nearest distance ( $d_{IB}$ ); extrapolation of the two probes ( $\mathbf{P}_1$  and  $\mathbf{P}_2$ ) from the IB cell ( $\mathbf{P}_{IB}$ ) and tri-linear interpolation of the temperature; and at last, a 1D interpolation of the temperature at  $\mathbf{P}_{IB}$  from the temperatures at  $\mathbf{P}_1$  and  $\mathbf{P}_2$ .

For the cells with centers inside the solid domain,  $flag=-1$ , and otherwise  $flag=1$ . Then the fluid cells ( $flag=1$ ) with at least one solid neighboring cell ( $flag=-1$ ) are identified as IB cells with  $flag=0$ , which are the green cells in Fig. 2(a) whose temperatures are interpolated from the surrounding non-solid/IB cells. To calculate the local surface normal direction, the  $\mathbf{P}_s$  at each particle surface is needed. For spheroids with symmetric axis, no analytical method for solving  $\mathbf{P}_s$  is available yet, so the iterative method of [28] is employed here. Both the flag assignment and  $\mathbf{P}_s$  calculation can be performed straightforwardly in the body-fixed coordi-

nate at each particle. To transform any location between the inertial ( $\mathbf{x}^I$ ) and body-fixed ( $\mathbf{x}^B$ ) coordinates, a rotation matrix,  $\mathbf{R}$ , is employed, with  $\mathbf{x}^B = \mathbf{R}\mathbf{x}^I$  and  $\mathbf{x}^I = \mathbf{R}^{-1}\mathbf{x}^B$ .  $\mathbf{R}$  is calculated based on a unit quaternion vector  $\mathbf{Q} = [Q_0, Q_1, Q_2, Q_3]$  by

$$\mathbf{R} = \begin{bmatrix} Q_0^2 + Q_1^2 - Q_2^2 - Q_3^2 & 2(Q_1 Q_2 + Q_0 Q_3) & 2(Q_1 Q_3 - Q_0 Q_2) \\ 2(Q_2 Q_1 - Q_0 Q_3) & Q_0^2 - Q_1^2 + Q_2^2 - Q_3^2 & 2(Q_2 Q_3 + Q_0 Q_1) \\ 2(Q_3 Q_1 + Q_0 Q_2) & 2(Q_3 Q_2 - Q_0 Q_1) & Q_0^2 - Q_1^2 - Q_2^2 + Q_3^2 \end{bmatrix} \quad (9)$$

The two probes,  $\mathbf{P}_1$  and  $\mathbf{P}_2$ , are extrapolated from the IB cell located in the direction ( $\mathbf{P}_{IB}-\mathbf{P}_s$ ) with  $|\mathbf{P}_2-\mathbf{P}_1|=|\mathbf{P}_1-\mathbf{P}_{IB}|=\Delta x$  [7,21] where  $\Delta x$  is the grid size for all three directions. The temperature values,  $T_1$  and  $T_2$ , at the two probes are tri-linear interpolated from the surrounding non-solid/IB cells in Fig. 2(b). With the interpolated temperature at the two probes  $\mathbf{P}_1$  and  $\mathbf{P}_2$ , the temperatures at the IB cell  $\mathbf{P}_{IB}$  is calculated based on the 2nd order interpolation functions [7,21]:

Dirichlet:

$$T_{IB} = \frac{[(d_{IB} - d_2)d_{IB}d_2 T_1 + (d_1 - d_{IB})d_{IB}d_1 T_2 + (d_{IB} - d_1)(d_{IB} - d_2)(d_1 - d_2)T_{s,im}]/[(d_1 - d_2)d_1 d_2]} \quad (10a)$$

Neumann:

$$T_{IB} = \frac{[(d_{IB}^2 - d_2^2)T_1 + (d_1^2 - d_{IB}^2)T_2 - (d_{IB} - d_1)(d_{IB} - d_2)(d_1 - d_2)(\partial T / \partial n)_{s,im}]/(d_1^2 - d_2^2)} \quad (10b)$$

where  $d_1 = |\mathbf{P}_1 - \mathbf{P}_s|$ ,  $d_2 = |\mathbf{P}_2 - \mathbf{P}_s|$ , and  $d_{IB} = |\mathbf{P}_{IB} - \mathbf{P}_s|$ .  $T_{s,im}$  and  $(\partial T / \partial n)_{s,im}$  are the imposed solid surface temperature and normal temperature gradient in prior. Accordingly, the local heat flux at particle surface,

$$q_s = -k(\partial T / \partial n)_s = -k[T_s(d_1^2 - d_2^2) + d_2^2 T_1 - d_1^2 T_2]/[(d_2 - d_1)d_1 d_2] \quad (11a)$$

and the solid temperature at  $\mathbf{P}_s$ ,

$$T_s = [(d_2 - d_1)d_1 d_2 (\partial T / \partial n)_s - d_2^2 T_1 + d_1^2 T_2]/(d_1^2 - d_2^2) \quad (11b)$$

Eqs. (11a) and (11b) are needed for calculating the heat transfer coefficient by a pair of  $q_s$  and  $T_s$  along with the computed temperature fields based on  $T_{IB}$  when imposing the Dirichlet and Neumann conditions, respectively.

Moreover, there are some special situations to be dealt with: For the probes: If  $\mathbf{P}_2$  is in the neighboring particles, the 1D interpolation is switched to the 1st order Taylor expansion. If both  $\mathbf{P}_1$  and  $\mathbf{P}_2$  are in the neighboring particles, the temperatures at these IB cells are assigned with the inlet temperature. For the tri-linear interpolated cells: If the tri-linear interpolated cells are the IB cells or in the solid phase (the neighboring particles), the temperature at these cells are assigned with the algebraically averaged value from the temperatures at the fluid cells of the total 8 (3D) cells around the probe. Note that the temperatures at these IB cells should not be used in the tri-linear interpolation, otherwise, due to the explicit time discretization in this work, the temperatures at the IB cell would continue to increase without a steady value. This is obviously not rational.

We have experienced no numerical instability in the simulation, even with no special treatment of the situations described above. The numerical stability of this method, coupling of DDF and GC in IBM, is same to DDF-IBM.

### 2.3. Outline of the algorithm

Based on Sections 2.1 and 2.2, the time integral of Eqs. (4) and (5) is implemented by the explicit 3rd Runge-Kutta scheme, where  $\gamma$  is the sub-step with 0 and 3 corresponding to the time steps  $n$  and  $n+1$ , respectively. The coefficients are:  $\alpha^1=32/60$ ,  $\beta^1=0$ ,  $\alpha^2=25/60$ ,  $\beta^2=-17/60$ ,  $\alpha^3=45/60$ ,  $\beta^3=-25/60$ .  $\mathbf{C}_u$  and  $C_T$  denote  $\rho\mathbf{u} \cdot \nabla \mathbf{u}$  and  $\rho c_p \mathbf{u} \cdot \nabla T$ , respectively.  $\mathbf{D}_u$  and  $D_T$  denote  $\nabla \cdot \{\mu[(\nabla \mathbf{u}) + (\nabla \mathbf{u})^T]\}$  and  $k\nabla^2 T$ , respectively. To properly enforce no-slip boundary condition at particle surface, the multidirect forcing scheme [29] is employed with the iteration number equal to 3. Overall, the procedure from time step  $n$  to  $n+1$  is summarized as:

for  $\gamma = 1$  to 3

Update temperature

Impose boundary condition at particle surface: update  $T^{\gamma-1}(\mathbf{P}_{IB})$  by GC-IBM, and update  $T^{\gamma-1}$  to  $T^\gamma$  as:

$$T^\gamma = T^{\gamma-1} + \Delta t / (\rho c_p) [\alpha^\gamma (D_T^{\gamma-1} - C_T^{\gamma-1}) + \beta^\gamma (D_T^{\gamma-2} - C_T^{\gamma-2})] \quad (12a)$$

Update velocity and pressure

Update  $\mathbf{u}^{\gamma-1}$  to  $\mathbf{u}^{\gamma-1,*}$  without  $\mathbf{f}$  as:

$$\begin{aligned} \mathbf{u}^{\gamma-1,*} = & \mathbf{u}^{\gamma-1} + \Delta t / \rho [-(\alpha^\gamma + \beta^\gamma) p^{\gamma-3/2} + \alpha^\gamma (\mathbf{D}_u^{\gamma-1} - \mathbf{C}_u^{\gamma-1}) \\ & + \beta^\gamma (\mathbf{D}_u^{\gamma-2} - \mathbf{C}_u^{\gamma-2})] \end{aligned} \quad (12b)$$

Impose boundary condition at particle surface: update  $\mathbf{u}^{\gamma-1,*}$  to  $\mathbf{u}^{\gamma-1,**}$  by DDF-IBM with  $\mathbf{f}$  in the immediate vicinity of particle surface [22] by the multidirect forcing scheme [29]:

Correct velocity and pressure:

$$\nabla^2 \phi = \rho_f / \Delta t \nabla \cdot \mathbf{u}^{\gamma-1,**} \quad (12c)$$

$$\mathbf{u}^\gamma = \mathbf{u}^{\gamma-1,**} - \Delta t / \rho_f \nabla \phi \quad (12d)$$

$$p^{\gamma-1/2} = p^{\gamma-3/2} + \phi \quad (12e)$$

end

The Navier-Stokes equations are solved by the finite volume scheme on a staggered 3D Cartesian grid, with a projection-correction method for the velocity-pressure decoupling in the momentum equations. The time propagation is discretized with the explicit 3rd order Runge-Kutta method [22], the convection terms  $\rho\mathbf{u} \cdot \nabla \mathbf{u}$  and  $\rho c_p \mathbf{u} \cdot \nabla T$  are discretized with the 2nd order upwind scheme, and the diffusion terms  $\nabla \cdot \{\mu[(\nabla \mathbf{u}) + (\nabla \mathbf{u})^T]\}$  and  $k\nabla^2 T$  are discretized with the 2nd order central differential scheme. The linear system of the pressure Poisson equations for  $\phi$  in Eq. (12c) is

solved by a multigrid-preconditioned conjugate gradient method (PFMG-CG) in the open source code HYPRE [30]. The full description of the algorithm is resumed in the flow-chart as shown in Fig. 3. Moreover, though the stability criterion may be complex in systems with moving spheroidal particles, e.g. [31], in static particle assemble systems, the criterion for CFL (Courant-Friedrichs-Lowy number) and von Neumann [22] stability is enough.

### 3. Simulation setup and analysis

DNS study of mean heat transfer coefficient with particle assemblies is challenging in that the fluid downstream will be heated up (or cooled down), so the fluid temperature sufficiently downstream will approach the particle surface temperature if the latter is fixed, which is termed saturation in the literature [7]. Flow at small  $Re$  and high  $\varphi$  is easier to saturate and yields statistically inhomogeneous streamwise heat transfer coefficient which is usually avoided by:

- keeping a constant temperature at the particle surface in tri-periodic domains including only developed heat transfer regions [3,4] and driving the fluid by a dynamically adjustable pressure gradient to a desired bulk Reynolds number;
- or keeping a constant temperature gradient at the particle surface [7] in dual-periodic domains with streamwise inlets and outlets but excluding the developing regions they induced in post-processing.

In the latter case, even for the same particle, the surface temperature varies with the surrounding fluid temperature. These two treatments will lead to different temperature distribution, but in fully-developed thermal condition and when saturation is weak, the spatial variation of the interphase heat flux in response to the temperature difference keeps similar in the streamwise direction which results in similar heat transfer coefficient (or Nusselt number) at each axial location. In this sense, they are identical for infinite random particle configurations. Thus, when the Nusselt number is to be studied, though simulations with a constant normal temperature gradient at the particle surface seem to deviate from those with a constant temperature, they produce similar Nusselt numbers.

In this work, the second treatment was used and the simulation setup is described in Fig. 4. The whole domain size is  $(25 \times 5 \times 5)d_e$  and the particle assembly spans from  $5d_e$  to  $15d_e$  in the  $x$ -direction (or namely flow direction) with a size of  $(L_x \times L_y \times L_z) = (10 \times 5 \times 5)d_e$ , so as to reduce the end effect of the flow on heat transfer. In the  $y$ - and  $z$ -directions, periodic boundary conditions are applied to both the fluid and solid phases for statistical homogeneity. In this work,  $Pr=0.74$ ,  $\varphi=0.1, 0.2, 0.3$ , and  $Re=2.5, 5, 10, 50, 100, 200$ . The particle number

$$N_p = 6\varphi \times (L_x \times L_y \times L_z) / (\pi d_e^3) \quad (13)$$

that is, 48, 96, and 144 particles at  $\varphi=0.1, 0.2$ , and 0.3, respectively.

In a cross-sectional slice at each axial location, the axial heat transfer coefficient,  $h(x)$ , is computed with the cross-sectionally averaged solid surface temperature  $\langle T_s \rangle(x)$  and the mixed-cup temperature  $\langle T_m \rangle(x)$ . With a constant heat flux  $q_{s,im}$  imposed at the particle surface,

$$h(x) = q_{s,im} / (\langle T_s \rangle(x) - \langle T_m \rangle(x)) \quad (14)$$

where

$$\langle T_s \rangle(x) = 1/l \int_l T_s dl \quad (15)$$

$$\langle T_m \rangle(x) = \int_{S_f} u T dS_f / \int_{S_f} u dS_f \quad (16)$$

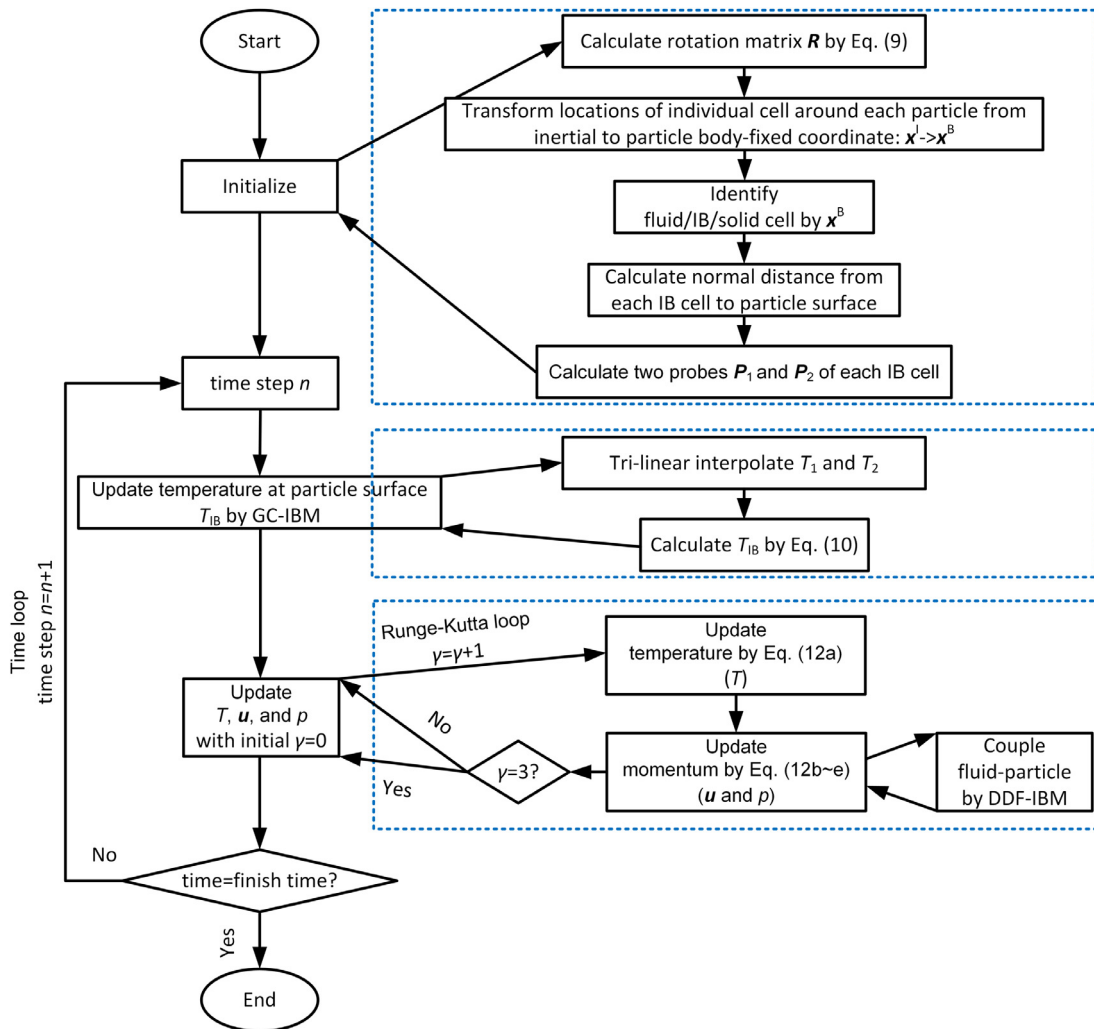


Fig. 3. Flow chart of the full algorithm.

where  $l$  is the perimeter length on the particle surface intersecting with the cross-sectional slice at  $x$  and  $dl$  is an element on it. Then the configuration-averaged axial heat transfer coefficient  $\{h\}(x)$  is calculated by further averaging  $h(x)$  over  $N_r$  random configurations to obtain

$$\{h\}(x) = \sum_{i=1:N_r} h(x)/N_r \quad (17)$$

It is then further averaged to obtain the overall heat transfer coefficient

$$h_{avg} = \int_{L_1}^{L_2} \{h\}(x) dx / (L_2 - L_1) = \sum_{i=1:N_r} \int_{L_1}^{L_2} h(x) dx / (L_2 - L_1) / N_r \quad (18)$$

where  $L_1$  and  $L_2$  are the distances of the start and end positions from the inlet. For gathering only the developed  $h(x)$ ,  $L_1 = 10d_e - 3d_e$  and  $L_2 = 10d_e + 3d_e$  are chosen, so the sampled-section length ( $L_2 - L_1$ ) is  $6d_e$ .  $Nu_{avg}$  was calculated by Eq. (1) with  $h_{avg}$  and gathered after the flow became steady.

The particles of different shapes were initialized with random locations and orientations in a computational domain expanded in the  $x$ -direction but having the final size in the  $y$ - and  $z$ -directions with periodic boundary conditions. Each particle was first assigned a virtual sphere with a radius of  $\max(a, c)$ , i.e., the maximum of its half axis length. The virtual spheres are randomly located in the initial domain with their volume fraction controlled at about 0.1 (so as to avoid successive overlapping and relocating). Then the

initial domain was squeezed in the  $x$ -direction to the final size of  $10d_e$  by two inward-moving fully-elastic end walls. The multi-sphere method was used to detect the non-spherical particle-particle or particle-wall collisions, the details of the multi-sphere method can be found in [17]. However, the rotation of the particles was prevented to keep their initial random orientations. To further smooth the fluctuation of the statistical results from this study,  $N_r$  configurations were generated for each set of parameters and each was simulated as an individual case. In Fig. 5, the symmetry axis vector is transformed from  $z$ -direction to a random-orientation vector by two sequence rotational angle  $\Lambda_1$  (azimuthal) and  $\Lambda_2$  (polar). The  $\Lambda_1$  is randomly seeded in the range  $[0, 180^\circ]$ . If the  $\Lambda_2$  is random, as approaching the poles in spherical coordinates, the density increases [32]. So according to [33], the  $\Lambda_2$  is generated by  $\arcsin(X)$  with  $X$  a random number between  $[0, 1]$  due to the symmetry of spheroid relative to its middle equatorial plane.

Then the quaternion vector can be constructed from the two rotational angles  $\Lambda_1$  and  $\Lambda_2$  [34,35]:

$$Q_0 = \cos(0.5\Lambda_2)\cos(0.5\Lambda_1) \quad (19a)$$

$$Q_1 = \sin(0.5\Lambda_2)\cos(0.5\Lambda_1) \quad (19b)$$

$$Q_2 = \sin(0.5\Lambda_2)\sin(0.5\Lambda_1) \quad (19c)$$

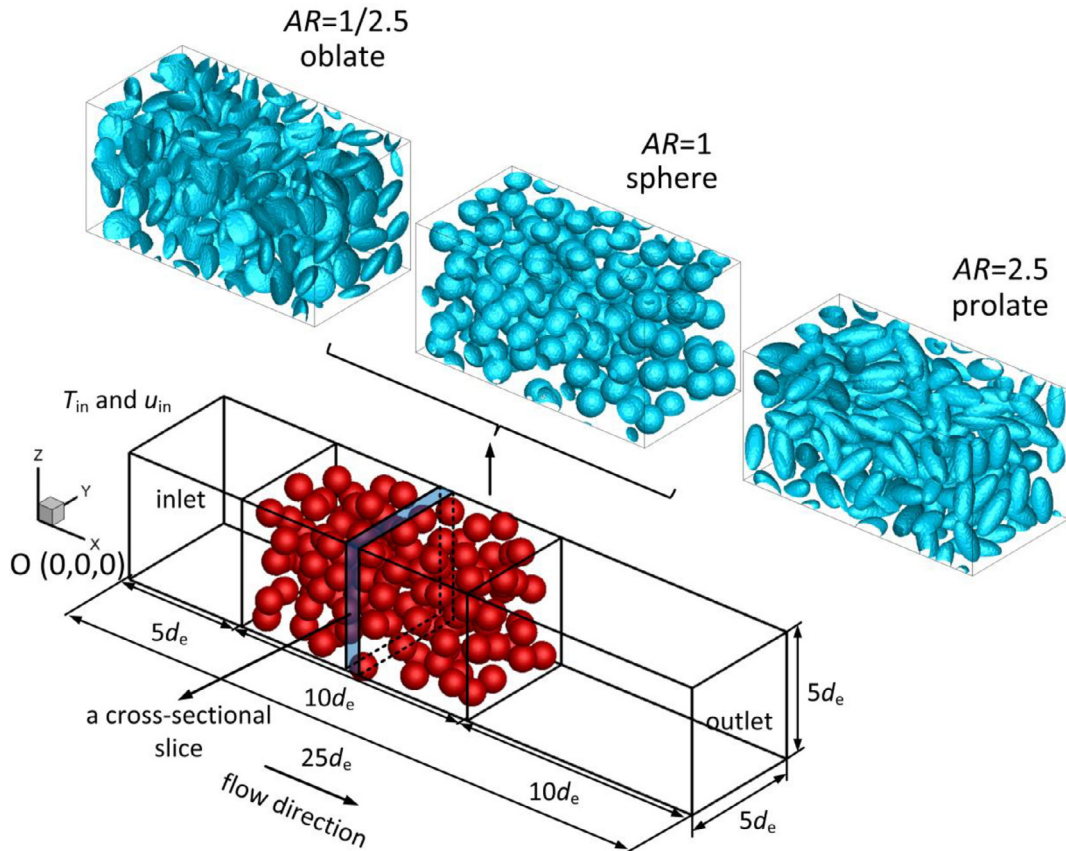


**Fig. 4.** Computational domain and typical particle configurations for the spheroids at  $\varphi=0.3$ .

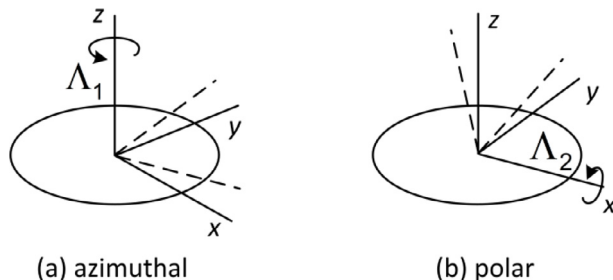


**Fig. 5.** Generation of the random orientation by two sequence rotations.

$$Q_3 = \cos(0.5\Lambda_2)\sin(0.5\Lambda_1) \quad (19d)$$

Based on the randomly-generated quaternion vector in Eq. (19), the transformations between the particle body-fixed coordinates and the inertial coordinates can be performed. The inclination angle,  $\Theta$ , is the intersection angle between the symmetry axis vector of a particle and a direction in the inertial coordinate. In Fig. 6(a), the frequency of  $\Theta$  with the  $x$ -,  $y$ -,  $z$ -directions for the random configuration scales with  $\sin(\Theta)$  [36]. While  $\cos(\Theta)$  presents uniform distributions. The same orientation dataset was shared by oblates and prolates. The Hermans orientation factor  $1/2(3(\cos^2(\Theta))_{\text{avg}} - 1)$  for these spheroid arrays is below 0.05, indicating good isotropy of the initial distributions.

#### 4. Validation and verification

Various aspects of the in-house code used in this work have been validated in our earlier papers [17,18]. In this section, we first

present a further validation in an isolated particle system for the hydrodynamic part (DDF-IBM) by drag coefficient and thermal part (GC-IBM) by Nusselt number. Next, we examine the numerical convergence of the heat transfer in the static particle assemblies designed above.

##### 4.1. Drag and heat transfer of isolated particle

To validate the numerical code before applying to the simulation cases designed above, the heat transfer of an isothermal hot particle in a cold fluid was simulated first in a domain of  $8d_e \times 8d_e \times 15d_e$  in size (similar to [13,37]) with  $Re=10, 50, 100$ , and  $Pr=0.74$ . The centroid of the particle was located at  $5d_e$  downstream from the inlet. A distance  $d_e$  was discretized with  $d_m$  uniform grid points in all  $x$ -,  $y$ -,  $z$ -directions.  $d_m$  was 40 in this validation test.

The boundary conditions were set as:

- No-slip and constant temperature ( $T_{p,s}=T_{s,in}$ ) at the particle surface;
- Constant velocity ( $u=u_{in}$ ,  $v=0$ , and  $w=0$ ) and constant temperature ( $T_{in}$ ) at the inlet;
- Zero gradient for velocities and temperature, and zero pressure at the outlet;
- Free-slip boundary condition spanwisely.

The drag coefficient  $C_D$  is defined as:

$$C_D = F_p / (1/2\rho u_{in}^2 S_c) \quad (20)$$

where  $F_p$  denotes the drag exerted on the particle and  $S_c$  is the equivalent cross-section area ( $1/4\pi d_e^2$ ).

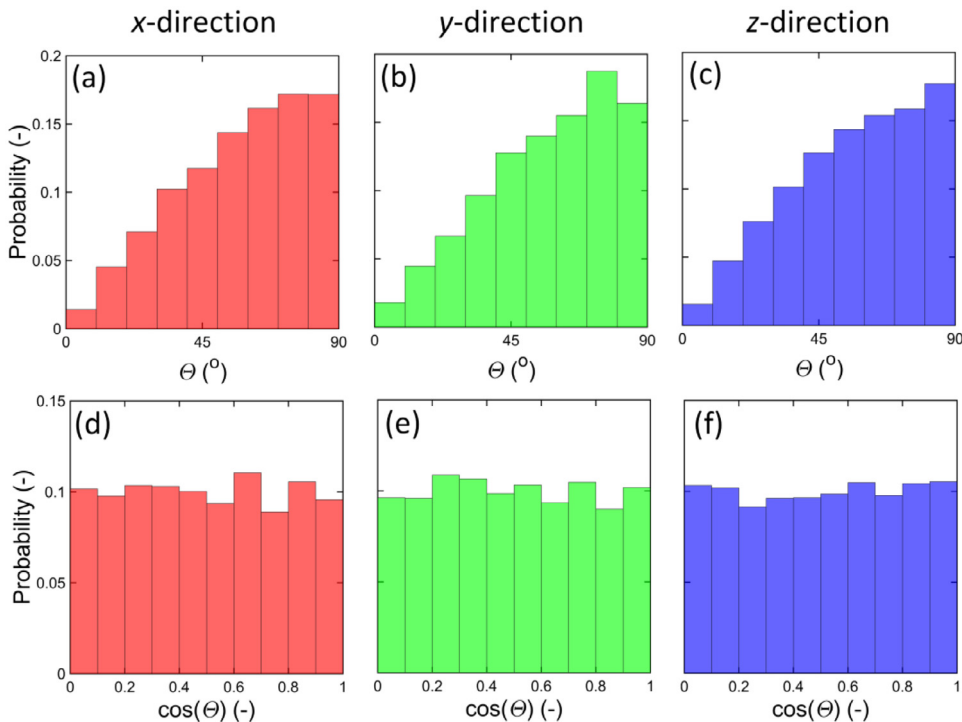


**Fig. 6.** Histogram of the particle inclination angles  $\Theta$  (top) with respect to the  $x$ -,  $y$ -,  $z$ -directions and  $\cos(\Theta)$  (bottom) for random configurations. (Only the results for  $\Theta=0\text{--}90^\circ$  are presented with similar distributions in the range of  $\Theta=180\text{--}90^\circ$  due to the symmetry.)

The particle Nusselt number  $Nu_p$  is calculated by Eq. (1) with the particle heat transfer coefficient  $h_p$  given by

$$h_p = q_p/S_p(T_{p,s} - T_{p,f}) \quad (21)$$

where the total heat transfer rate  $q_p$  is obtained by integrating  $q_s$ , from Eq. (11a), over the surface of a particle.  $T_{p,f}$  is the fluid-averaged temperature given by

$$T_{p,f} = \frac{\int T dV_f}{V_f} \quad (22)$$

with  $V_f$  the fluid volume. In Fig. 7(a), the  $C_D$  of the sphere agrees well with both the numerical and experimental literature data [13,38]. Moreover, at  $Re=100$ , the results of prolates and oblates versus the inclination angle  $\Theta$  are shown in Fig. 7(b), which agree well to [13] with  $C_D$  and  $\Theta$  positively and negatively correlated for  $AR=2.5$  (prolates) and 0.5 (oblates), respectively.

As to heat transfer for sphere, the prior DNS data [13,14,39] and the correlations of Ranz and Marshall [40], Whitaker [41], and Feng and Michaelides [42], that is,

$$Nu_{p,\text{pre}} = 2.0 + 0.6Re^{0.5}Pr^{0.33} \quad (23a)$$

$$Nu_{p,\text{pre}} = 2.0 + (0.4Re^{0.5} + 0.06Re^{2/3})Pr^{0.4} \quad (23b)$$

$$Nu_{p,\text{pre}} = 0.992 + Pe^{1/3} + 0.1Re^{1/3}Pe^{1/3}, \text{ where } Pe = Re \times Pr \quad (23c)$$

are compared with the computed results in Fig. 7(c). They are in good agreement but, in general, the deviation to the literature results is negative and its magnitude increases with  $Re$  due to the decreasing thickness of thermal boundary layers which cannot be properly resolved at  $d_m=40$ . For spheroidal particles, e.g., prolates of  $AR=2$  and 2.5, at  $Re=100$  in Fig. 7(d), the trend of  $Nu_p$  versus  $\Theta$  agrees to [13,14] with the relative deviation at 10% roughly, similar to that of spheres at  $Re=100$  in Fig. 7(c).

#### 4.2. Convergence study of particle assemblies

Numerical convergence is obviously a source of uncertainty, which is affected by  $d_m$ ,  $CFL$ , and  $N_r$ . So to examine their effects, the results in particle assemblies with different  $d_m$  at high  $Re$  are first compared in Fig. 8. All the results for three particle shapes at  $Re=100$  converge as  $d_m$  is increased up to 80, but this resolution is computationally infeasible currently. In particular, the results at  $Re=200$  do not converge even at  $d_m=80$ . Though the results in this work are not strictly grid independent, they are still meaningful to us for the following reasons:

- In the literatures [4,7], the maximum  $d_m=40$  was usually adopted. So to keep consistency with them,  $d_m=40$  for  $Re=100$  and  $d_m=50$  for  $Re=200$  have been adopted.
- With a large number of simulation cases (54 cases with 5 configurations for each case), we have to compromise between accuracy and computational cost.
- More importantly, as similar orders of convergence are found for different particle shapes, the relative magnitudes of  $Nu_{\text{avg}}$  may well reflect their real ranking at the grid independent limit, and this is sufficient for the purpose of this study.
- Moreover, as argued by Sun et al. [4], the discrepancy due to the grid-dependence at the current resolution may be up to 10% in the studied parameter region, but this is much smaller than the experimental results (scatter over several orders of magnitude). So this kind of DNS can already provide more certainty to our understanding of the shape effect.

Next, as listed in Table 2, for spheres at  $\varphi=0.3$  and  $Re=100$ , as  $CFL$  increases from 0.25 to 1,  $Nu_{\text{avg}}$  decreases by only 1%, which is negligible. So in this work, all the cases are simulated with  $CFL<0.5$  by default. Moreover, the choose of the Dirichlet (isothermal) and Neumann (isoflux) boundary conditions at particle surface also affects the heat transfer, and thus  $Nu_{\text{avg}}$ . From the comparative cases at  $\varphi=0.1\&Re=5$ ,  $\varphi=0.1\&Re=100$ , and  $\varphi=0.3\&Re=100$ , the smaller relative error is at  $\varphi=0.1\&Re=100$  with a magnitude

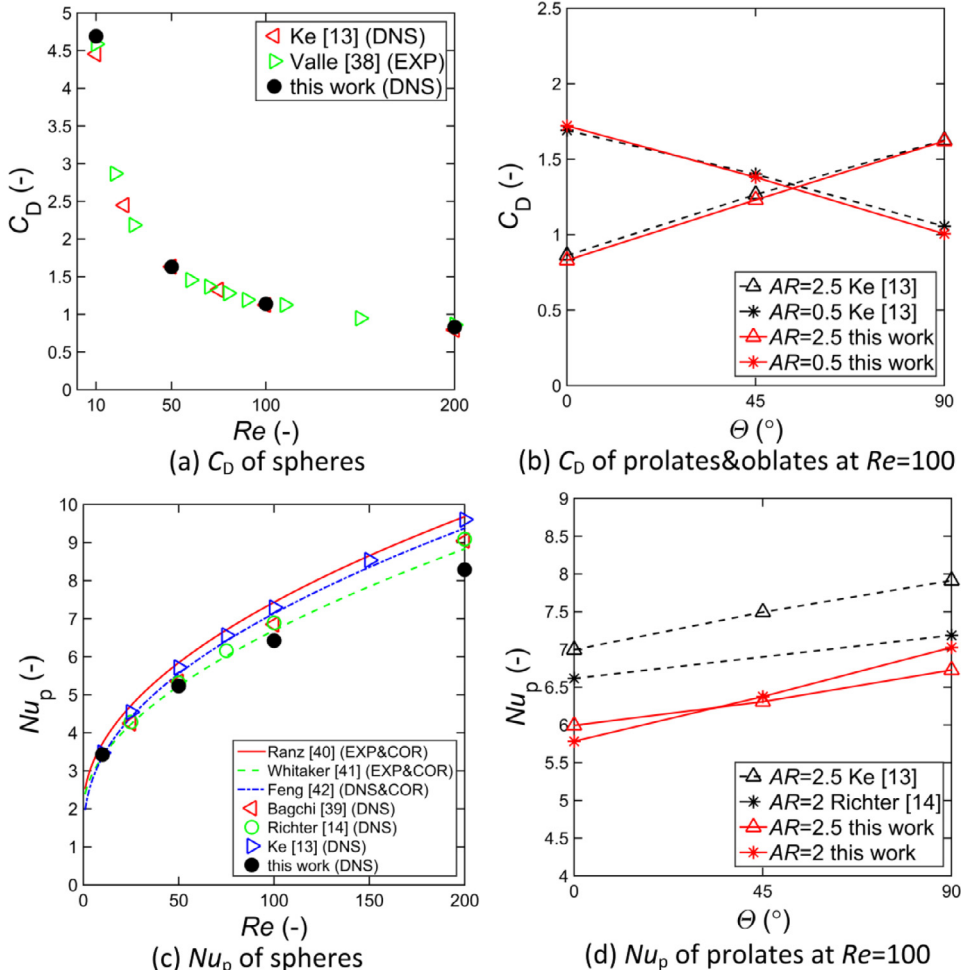


**Fig. 7.**  $C_D$  and  $Nu_p$  versus  $Re$  for spheres and  $\Theta$  at  $Re=100$  for prolates and oblates.  
(EXP and COR denote experiments and correlations, respectively.)

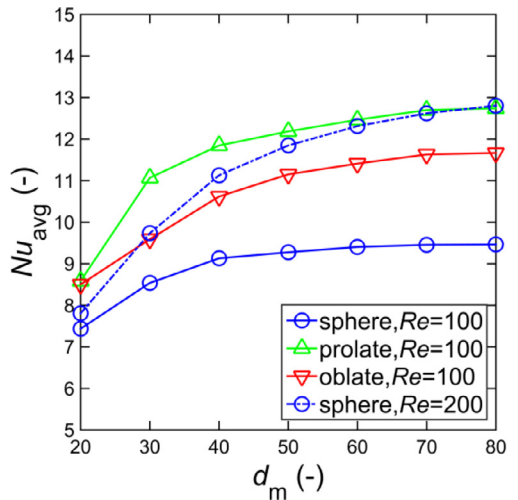


**Fig. 8.** Variation of  $Nu_{avg}$  versus  $d_m$  at  $Re=100$  and  $200$  with  $\varphi=0.3$ .

of  $O(0.5\%)$ . It indicates that the  $Nu_{avg}$  are almost identical for the Neumann and Dirichlet boundary conditions when the saturation effect is weak at low  $\varphi$  and high  $Re$ . For instance, at  $\varphi=0.3$ , the relative error at  $Re=100$  is smaller than that at  $Re=5$  due to the weaker saturation effect at higher  $Re$ . With the Dirichlet condi-

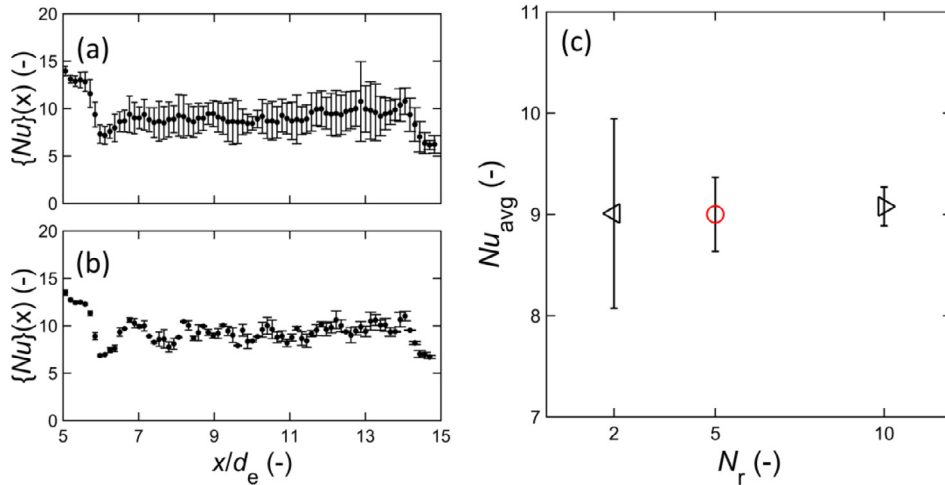
**Table 2**  
Effects of boundary condition at particle surface and CFL on  $Nu_{avg}$ .

$Nu_{avg}$ and relative error $E$	$\varphi=0.1$		$\varphi=0.3$		CFL
	$Re=5$	$Re=100$	$Re=5$	$Re=100$	
Sphere	Neumann	2.69	7.33	-	9.16
	Dirichlet	3.04	7.34	-	9.11
	$E$	13.0%	0.1%	-	9.05
Prolate	Neumann	3.02	8.13	-	9.99
	Dirichlet	3.40	8.15	-	11.83
	$E$	12.6%	0.2%	-	0.5
Oblate	Neumann	2.52	7.67	-	12.00
	Dirichlet	2.84	7.61	-	10.60
	$E$	12.7%	-0.8%	-	0.5

(At  $\varphi=0.3$  and  $Re=5$ , no data is listed in the column due to the strong saturation effect with the Dirichlet at high  $\varphi$  and low  $Re$ ;  $E=(Nu_{avg,Dirichlet}-Nu_{avg,Neumann})/Nu_{avg,Neumann}$  at  $CFL=0.5$ .)

tion, when the saturation is strong at  $\varphi=0.3$  or low  $Re$ , the  $h(x)$  increases with  $x$  significantly (not shown here for brevity), i.e., the downstream  $h(x)$  is larger, resulting in higher  $Nu_{avg}$  which is to be avoided in the post-processing of  $Nu_{avg}$ . Therefore, the discussions in Section 5 later are all about the simulation with the Neumann (isoflux) boundary condition.

On the other hand, similar to [3], the effect of  $N_r$  was studied for spheres at  $\varphi=0.3$  and  $Re=100$  in Fig. 9. The standard er-

Fig. 9. Effect of  $N_r$  on the Nusselt number.

**Table 3**  
Cases number under various conditions.

$\varphi$	$N_p$	AR	Re					
			2.5	5	10	50	100	200
0.1	48	1	1	2	3	4	5	6
		2.5	19	20	21	22	23	24
		0.4	37	38	39	40	41	42
0.2	96	1	7	8	9	10	11	12
		2.5	25	26	27	28	29	30
		0.4	43	44	45	46	47	48
0.3	144	1	13	14	15	16	17	18
		2.5	31	32	33	34	35	36
		0.4	49	50	51	52	53	54

ror of  $\{Nu\}(x)$ , calculated by Eq. (1) with  $\{h\}(x)$ , indicated by the 95% confidence intervals, is significantly reduced as  $N_r$  is increased from 2 (Fig. 9(a)) to 10 (Fig. 9(b)). The variation of the mean standard error from  $N_r=2$  to 10 can also be observed intuitively in Fig. 9(c). As the computational cost increases linearly with  $N_r$ ,  $N_r=5$  was chosen in this work.

## 5. Results and discussion

The simulation cases are specified in Table 3, based on which the overall characteristics is first analyzed. Second, the  $Nu_{avg}$  for spheres and prolates are compared to the prior DNS data and correlations in literature. Third, the effect of particle shape on  $Nu_{avg}$  is examined and new correlations for prolates and oblates are proposed. At last, the  $Nu_{avg}$  for several specific particle orientations at low  $Re$  is presented to indicate that the relationship between the  $Nu_{avg}$  of prolates and oblates is robust and insensitive to the lack of perfect randomness in their orientations due to the limited number of configurations ( $N_r=5$ ). In all cases,  $\rho$ ,  $d_e$ ,  $u_{in}$ , and  $q_{s,im}d_e/k$  are taken as the units of density, length, velocity, and temperature, respectively, and the time step is then chosen to achieve  $CFL<0.5$ . All data were collected at the time equivalent to approximate 1.5 flow-through time, defined by  $L_x/u_{in}$ , when  $Nu_{avg}$  became steady with further computation for another flow-through time resulting in a relative decrease of  $Nu_{avg}$  less than 0.1%.

### 5.1. Overall velocity and temperature fields

Fig. 10 shows the velocity and temperature fields for the three particle shapes. As a positive constant heat flux is applied at im-

mersed solid surface in this work, fluid temperature increases as it flows through the packed region. By comparing the velocity and temperature fields in Fig. 10(a)(c)(e) and (b)(d)(f), a strong correlation can be found between the regions of high velocity and low temperature and vice versa, yielding high and low heat transfer coefficients, respectively. In general, the temperature at the immersed surface increases in the flow direction as the temperature of the fluid surrounding the particle increases. On most particles, the windward side exhibits lower surface temperatures because of flow impingement and higher heat transfer coefficients, whereas the downwind or wake side exhibits higher temperatures. Compared to single-phase flow, particle wake modifies the hydrodynamics, and thus the heat transfer from two aspects: (1) When a particle lies in the wake of another particle, the low velocity in the wake will reduce the effective interstitial Reynolds number and heat transfer coefficient on the particle. This could be understood as blocking, a local phenomena; (2) Interactions between the wake and other particles induce mixing, a global phenomena. The overall heat transfer characteristics is determined by these two coexisting mechanisms. The transverse inhomogeneity of the wake distribution results in channeling which weakens mixing, e.g., the higher velocity and lower temperature as shown in the white dashed ellipse in Fig. 10(a)(b) for spheres, which is weaker for non-isotropic particles (prolates and oblates) in Fig. 10(c)~(f). In other words, non-isotropic particle can improve mixing. Moreover, for oblates, the temperature in Fig. 10(f) is obviously higher than the other two shapes. It could be caused by the larger wake area in Fig. 10(e) when their symmetry axis is aligned with the  $x$ -direction. Quantitatively, Fig. 11 shows the slice-averaged temperature distribution. It can be observed that both  $\langle T_s \rangle(x)$  and  $\langle T_m \rangle(x)$  are higher for oblates than those for spheres and prolates, which is consistent with the contour in Fig. 10. It should be noted that  $\langle T_s \rangle(x) - \langle T_m \rangle(x)$  is inversely proportional to the heat transfer rate under the boundary condition of constant heat flux at particle surface. Its values are smaller for prolates and oblates resulting in their higher heat transfer rate compared to spheres which is consistent with the  $Nu_{avg}$  behavior in Section 5.3.

To understand the blocking further, a blockage factor,  $A_i$ , is introduced with reference to [5,43]. As illustrated in Fig. 12, it is the upwind surface fraction axially shadowed by the solid cells within an axial distance of  $d_e$  to the particle surface considered. Accordingly, the upstream effective velocity,  $u_{eff,i}$ , is defined as an average of the interstitial fluid velocity in the fluid region  $V_i$  upstream of particle  $i$ , as schematically shown by the shaded region

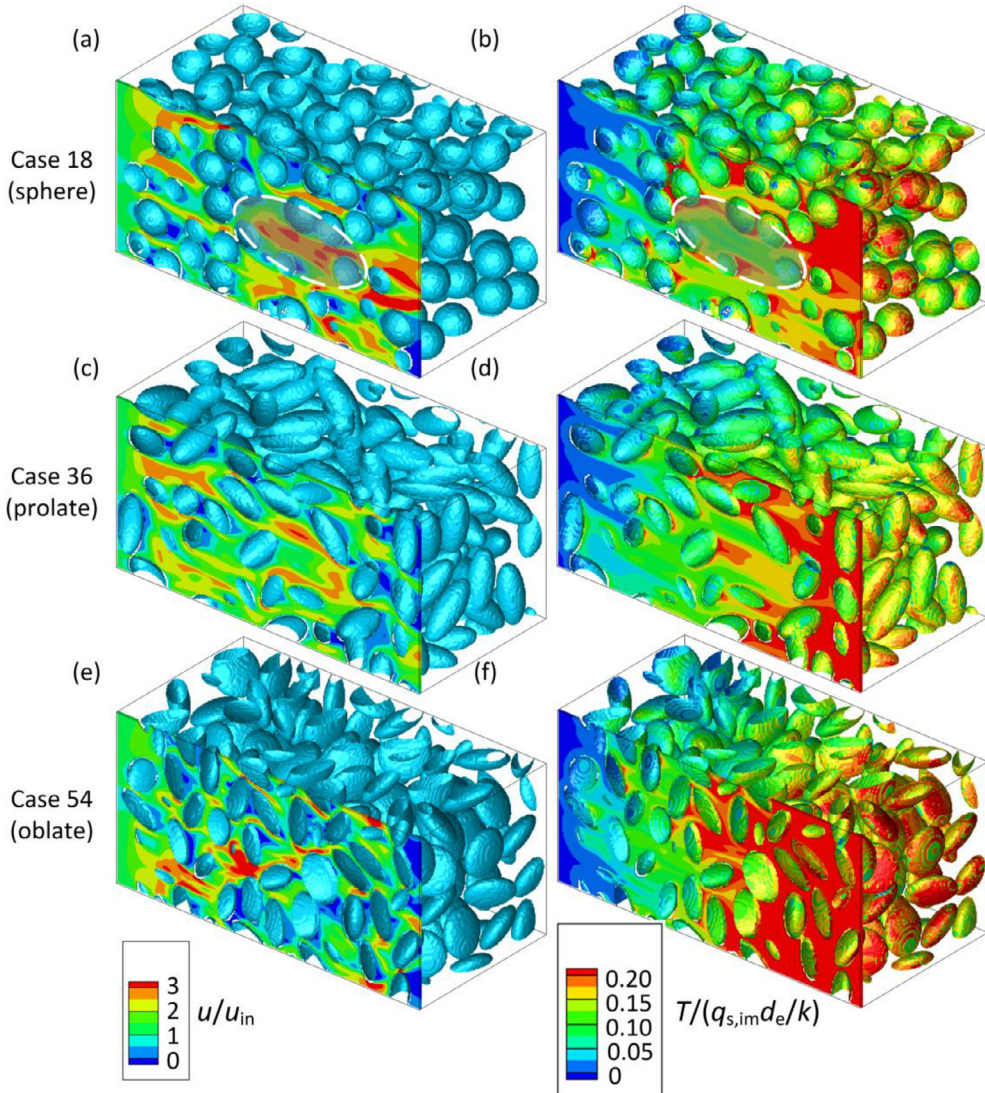


**Fig. 10.** Contours of the dimensionless axial velocity (a)(c)(e) and temperature (b)(d)(f) at  $Re=200$  and  $\varphi=0.3$ . (In (b)(d)(f), the particle surfaces are also colored by the temperature.)

in Fig. 12,

$$u_{\text{eff},i} = \frac{\int u dV_i}{V_i} / V_i \quad (24)$$

As shown by the probability density function (PDF) of  $A_i$  in Fig. 13(b), for  $\varphi=0.3$ , oblates have the largest average  $A_i$ , so the highest temperature observed for oblates in Figs. 10 and 11 may be attributed to this most severe blocking which produces the strongest wakes. For  $Re=200$ , Fig. 13(c)(d) shows the PDF of  $u_{\text{eff},i}/u_{\text{in}}$ . It seems that prolates have the narrowest PDF of  $u_{\text{eff},i}/u_{\text{in}}$  which indicates better mixing. Fig. 13(e)(f) shows that  $u_{\text{eff},i}/u_{\text{in}}$  decreases with the increase of  $A_i$  in a statistical sense. It confirms quantitatively that more severe blocking leads to weaker convection.

## 5.2. Comparison with prior DNS data and correlations

To understand the overall heat transfer behavior and to further validate the DNS results, they are compared to the literature results listed in Table 4 including the experimental correlation of Gunn [1] and the numerically developed correlations as well as the corresponding DNS data from Tavassoli et al. [2,44] and Sun

et al. [4] for spheres and He and Tafti [7] for both spheres and prolates, respectively. In these correlations, the voidage  $\varepsilon$  has been used which equals to  $1-\varphi$ .

As shown in Fig. 14, all the literature data and the associated correlations exhibit a consistent trend: When  $\varphi$  is given,  $Nu_{\text{avg}}$  increases with increasing  $Re$  due to the increased heat transfer coefficient. Similarly, at given  $Re$ , the  $Nu_{\text{avg}}$  increases with increasing  $\varphi$ . Note that  $Re$  is defined based on the superficial velocity, so when  $\varphi$  increases, the interstitial velocity also increases, which contribute to the increase of  $Nu_{\text{avg}}$ . For the spheres, this work supports the results of [4,7] and of [2,44] at  $Re \leq 10$  for all  $\varphi$  values considered. Note that as  $Re$  increases, the  $Nu_{\text{avg}}$  of [2,44] shows faster increase than that in [4,7] and this work. This discrepancy has been reported by Sun et al. [4] and He and Tafti [7] also, who attributed it to the inadequate length of the thermal developing region at the entrance of [2,44], especially at higher  $Re$ . For  $Re=200$ , this work obtained higher  $Nu_{\text{avg}}$  than [7] for spheres at all values of  $\varphi$ , but agrees well with Sun's correlation [4]. In general,  $Nu_{\text{avg}}$  is more sensitive to the numerical method and grid resolution used at higher  $Re$ , and this may explain the discrepancy among these results. For the prolates at  $\varphi=0.3$ , as  $Re$  decreases, our  $Nu_{\text{avg}}$  is significantly higher than that of [7] at low  $Re$  and high  $\varphi$ , as shown in

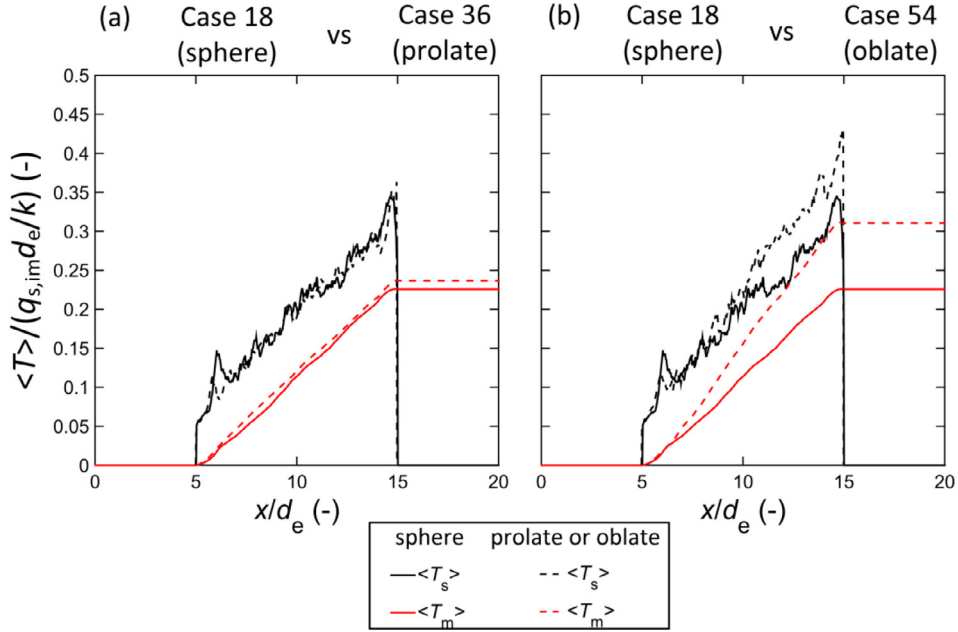


Fig. 11. Variation of the dimensionless  $\langle T_s \rangle(x)$  and  $\langle T_m \rangle(x)$  versus  $x/d_e$  at  $Re=200$  and  $\varphi=0.3$

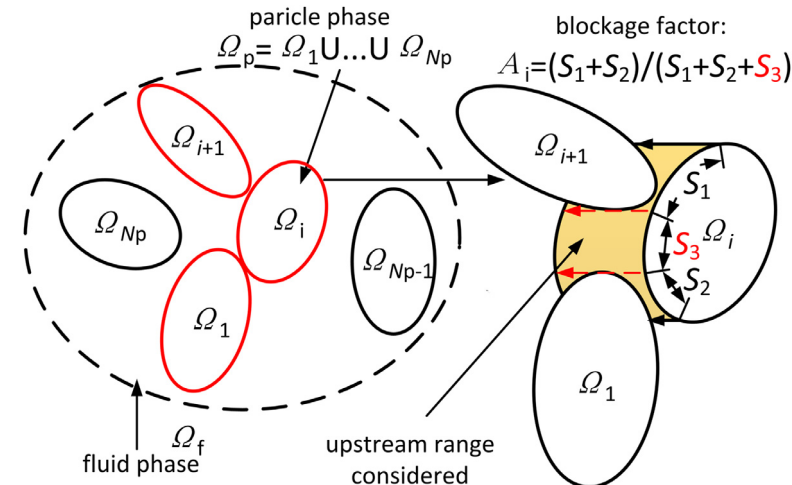
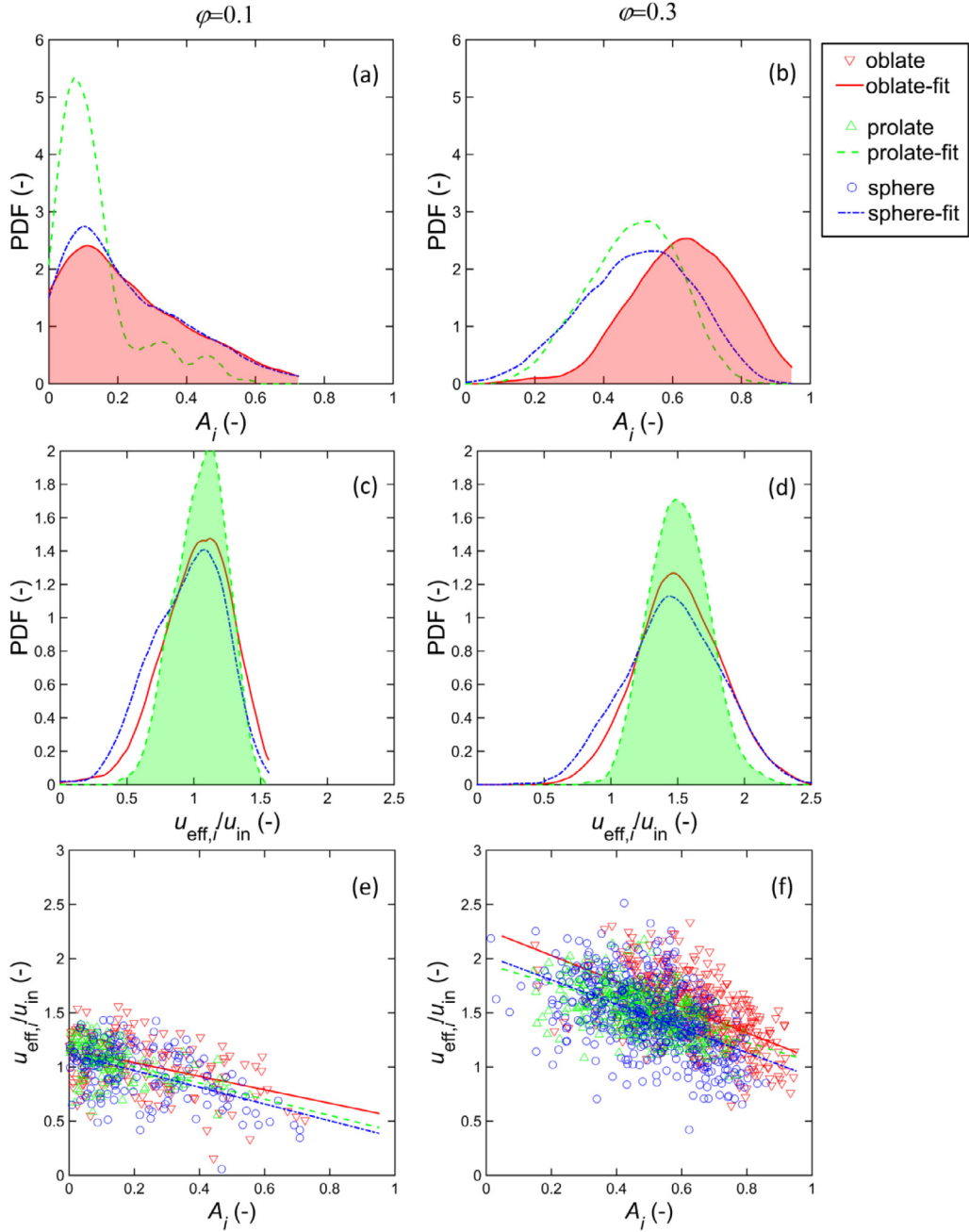


Fig. 12. Schematics of the upstream region and blockage factor.

**Table 4**  
The correlations in literature and their applicable ranges.

Correlation	$Re$	$\varepsilon$ (or $1-\varphi$ )	Particle shape	$Nu_{avg,pre}$
Gunn [1]	$1 \leq Re \leq 10^5$	$0.35 \leq \varepsilon < 1.0$	Sphere	(a)
Tavassoli et al. [44]	$10 \leq Re \leq 100$	$0.50 \leq \varepsilon \leq 0.9$	Sphere	(b)
Sun et al. [4]	$1 \leq Re \leq 100$	$0.50 \leq \varepsilon \leq 0.9$	Sphere	(c)
He and Tafti [7]	$10 \leq Re \leq 200$	$0.65 \leq \varepsilon \leq 0.9$	Prolate	(d)

$$\begin{aligned}
 (a) \quad & (7 - 10\varepsilon + 5\varepsilon^2)(1 + 0.7Re^{0.2}Pr^{1/3}) + (1.33 - 2.4\varepsilon + 1.2\varepsilon^2)Re^{0.7}Pr^{1/3}; \\
 (b) \quad & (7 - 10\varepsilon + 5\varepsilon^2)(1 + 0.1Re^{0.2}Pr^{1/3}) + (1.33 - 2.19\varepsilon + 1.15\varepsilon^2)Re^{0.7}Pr^{1/3}; \\
 (c) \quad & (-0.46 + 1.77\varepsilon + 0.69\varepsilon^2)/\varepsilon^3 + (1.37 - 2.4\varepsilon + 1.2\varepsilon^2)Re^{0.7}Pr^{1/3}; \\
 (d) \quad & (1.49 - 0.885\varepsilon + 0.078\varepsilon^2)(2.458 - 0.042Re^{1.09}Pr^{1/3}) + (1.114 - 0.62\varepsilon - 0.08\varepsilon^2)Re^{0.7}Pr^{1/3}.
 \end{aligned}$$



**Fig. 13.** PDFs of  $A_i$  (top) and  $u_{\text{eff},i}/u_{\text{in}}$  (middle) and variation of  $u_{\text{eff},i}/u_{\text{in}}$  versus  $A_i$  (bottom) at  $\varphi=0.1$  and 0.3. (The trend lines are fitted by the least-square method.)

the black dashed circle in Fig. 14(b). It is probably due to the sensitivity of  $Nu_{\text{avg}}$  to particle orientation under such conditions. Fortunately, this discrepancy does not change the relative magnitudes of  $Nu_{\text{avg}}$  for different particle shapes, which justifies the discussions in the following subsection.

### 5.3. Effect of particle shape

To investigate the effect of particle shape, the variation of  $Nu_{\text{avg}}$  with  $Re$  and  $\varphi$  are plotted in Fig. 15 as correlations based on the form originally proposed by Gunn [1] with the coefficients in the  $\varepsilon$ -dependent groups adopted from [7], and the coefficients of the  $Re$ -dependent groups in the first term fitted by the least-square method resulting in average relative errors below 5%. The corre-

lations are, for oblates,

$$\begin{aligned} Nu_{\text{avg,pre}} = & (1.49 - 0.885\varepsilon + 0.078\varepsilon^2)(2.506 - 0.084Re^{0.982}Pr^{1/3}) \\ & + (1.114 - 0.62\varepsilon - 0.08\varepsilon^2)Re^{0.7}Pr^{1/3} \end{aligned} \quad (25)$$

and for prolates, though a correlation was proposed by He and Tafti [7], its deviation from our DNS data cannot be ignored for low  $Re$  at high  $\varphi$ , which is probably due to the sensitivity to particle orientations under such conditions. Considering both the best fit and brevity, we correlate the three coefficients of the  $Re$ -dependent groups in the first term to  $\varepsilon$  as:

$$\begin{aligned} Nu_{\text{avg,pre}} = & (1.49 - 0.885\varepsilon + 0.078\varepsilon^2)(C_1 + C_2Re^{C_3}Pr^{1/3}) \\ & + (1.114 - 0.62\varepsilon - 0.08\varepsilon^2)Re^{0.7}Pr^{1/3} \end{aligned} \quad (26)$$

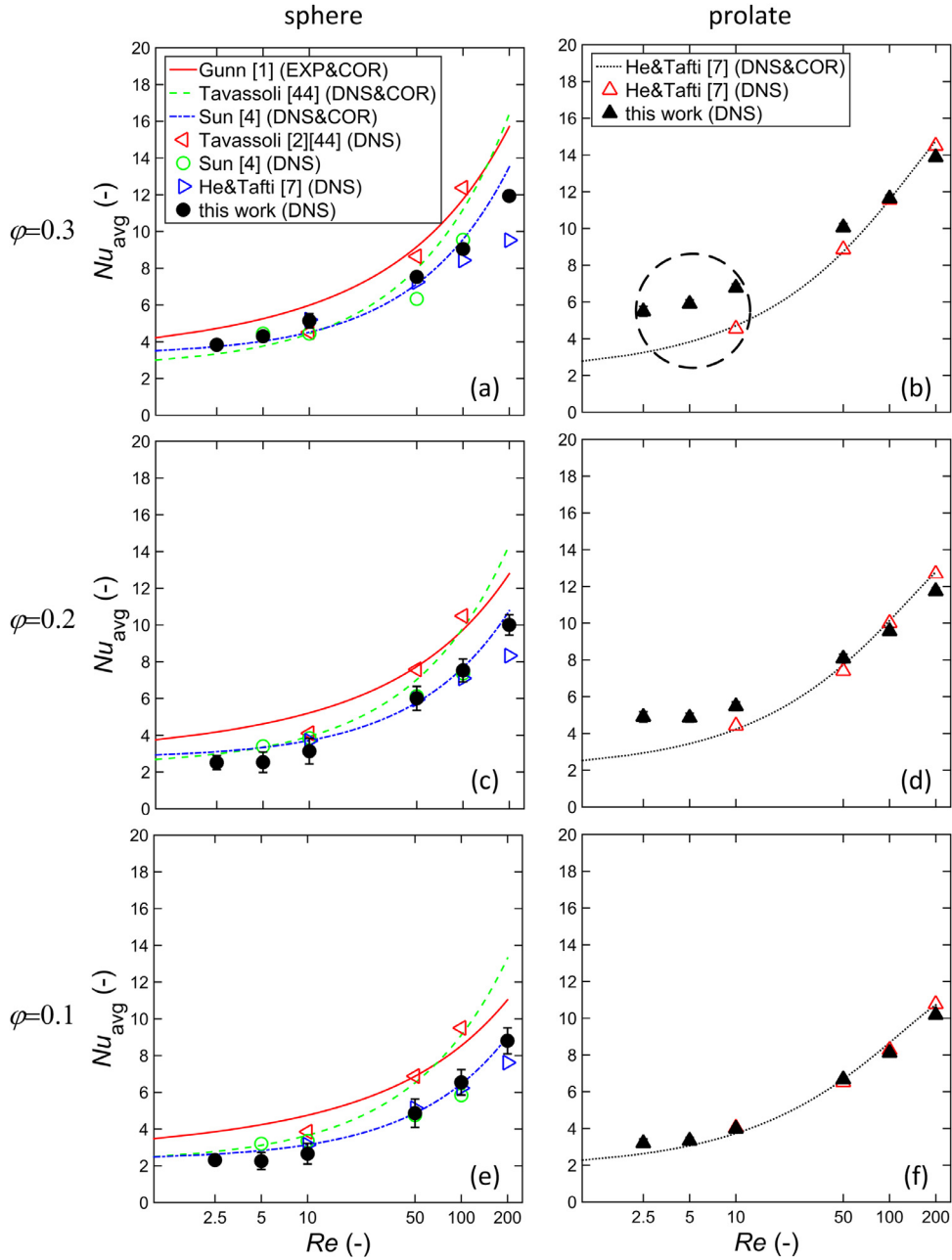


**Fig. 14.** Comparison of the  $Nu_{avg}$  with the DNS data and correlations in literature. (Symbols indicate the  $Nu_{avg}$  and the error bars indicate 95% confidence intervals.)

where  $C_1$ ,  $C_2$ , and  $C_3$  are linear functions of  $\varepsilon$ , that are,

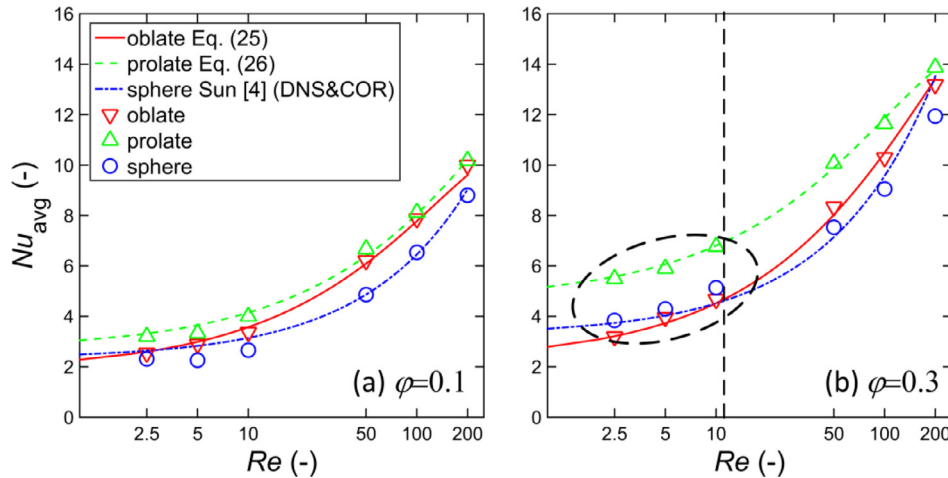
$$C_1 = 10.603 - 7.8053\varepsilon \quad (27a)$$

$$C_2 = 0.1014 - 0.2847\varepsilon \quad (27b)$$

$$C_3 = 1.3710 - 0.5571\varepsilon \quad (27c)$$

As shown in Fig. 15, in the moderate  $Re$  range ( $10 \leq Re \leq 200$ ) or at low  $\varphi$  (e.g., 0.1), the  $Nu_{avg}$  of both prolates and oblates are higher than spheres. Whereas at high  $\varphi$  (e.g., 0.3) and low  $Re$  (e.g.,  $<5$ ), the  $Nu_{avg}$  of oblates is lower than spheres as shown in the black dashed ellipse in Fig. 15(b). By comparing the correlations

for spheres [4] to Eq. (25) for oblates and Eq. (26) for prolates, the intersections of the  $Nu_{avg}$  curves of oblates and spheres can be found roughly at  $Re=10$  for  $\varphi=0.3$ . Meanwhile, for the range of  $\varphi$  considered, the difference between prolates and oblates narrows as  $Re$  increases and literally vanishes at  $Re=200$ . It can be reasonably expected that, at even higher  $Re$  (though not studied yet due to computational cost), the  $Nu_{avg}$  of oblates may be higher than prolates. In a word, in the studied range of  $\varphi$  and  $Re$ , compared to spheres, prolates intensify the heat transfer most. While at high  $\varphi$ , the heat transfer for oblates is sensitive to  $Re$ , which is attenuated and intensified at low and high  $Re$ , respectively. This is further explained in Section 5.4.

Fig. 15. Variation of  $Nu_{avg}$  with  $Re$  in different cases.

**Table 5**  
 $Nu_{avg}$  for different specific orientation configurations at  $Re=5$ .

$Nu_{avg}$ and relative error $E$		$\varphi=0.1$	$\varphi=0.3$
Fully random (reference)	Prolate Oblate $E$	3.33 2.90 14.83%	5.90 3.96 48.99%
Plane-x random	Prolate Oblate $E$	3.36 3.03 10.89%	5.63 4.69 20.04%
Plane-y/z random	Prolate Oblate $E$	3.53 2.69 31.23%	5.85 3.78 54.76%
Orientation-x	Prolate Oblate $E$	3.26 2.58 26.36%	5.21 3.54 47.18%
Orientation-y/z	Prolate Oblate $E$	3.55 2.84 25.00%	5.10 3.91 30.43%

$$(E = (Nu_{avg,prolate} - Nu_{avg,oblate}) / Nu_{avg,oblate}).$$

#### 5.4. Effect of particle orientation at low $Re$

In the previous sections, the heat transfer has been studied in the static assemblies of particles with random locations and orientations. Of course, particle orientation may also affect the heat transfer rate. Motivated by this consideration, we have performed additional simulations with specific orientations. For plane-x random configurations, the distribution of  $\Theta$  with respect to  $y/z$ -direction is flat, presenting a uniform distribution in Fig. 16(a), whereas the distribution of  $\cos(\Theta)$  is non-uniform with higher density as approaching 1 in Fig. 16(b). The same trends hold for plane-y random configurations except that the  $\Theta$  is respect to  $x/z$ -direction. Their results suggest that the orientation effect is con-

siderably strong at low  $Re$  while it is negligible at high  $Re$ . So the results at  $Re=5$  are summarized in Table 5, which shows that, for all the orientations studied, the  $Nu_{avg}$  for prolates is significantly higher than that for oblates. So the relationship found in cases with fully random orientations in the previous sections still holds for other specific orientations. Moreover, the dependence of heat transfer on the  $Re$  at high  $\varphi$  discussed in Section 5.3 can be explained by Fig. 17 where the  $Nu_{avg}$  for various specific orientations at  $\varphi=0.3$  (Fig. 17(a)(b)) and the corresponding axial profiles of configuration&cross-sectionally averaged solid surface temperature  $\{\langle T_s \rangle\}_x$  (Fig. 17(c)(d)) are plotted. Different from prolates in Fig. 17(b), for oblates in Fig. 17(a), the  $Nu_{avg}$  for fully random orientations (enclosed by dashed circle) is even comparable to that in

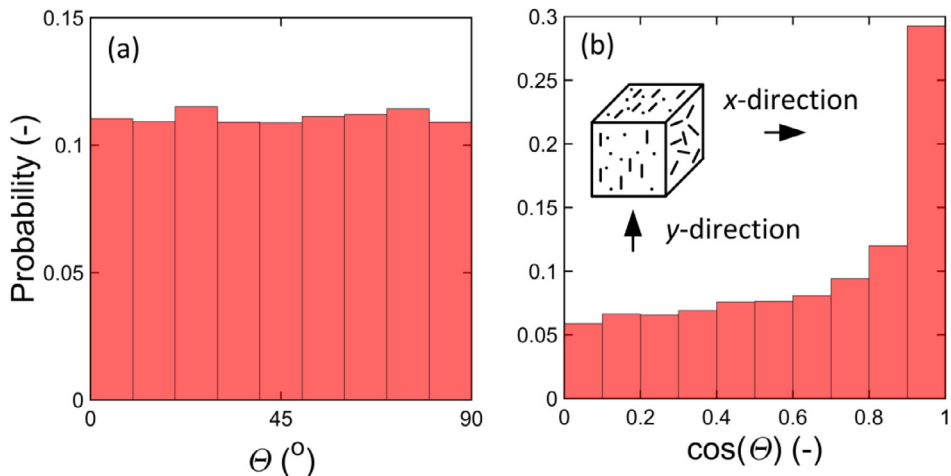


**Fig. 16.** Histogram of the particle inclination angles  $\Theta$  and  $\cos(\Theta)$  for plane-x random configurations.  
(Only the results for  $\Theta=0\text{--}90^\circ$  are presented with similar distributions in the range of  $\Theta=180\text{--}90^\circ$  due to the symmetry.)

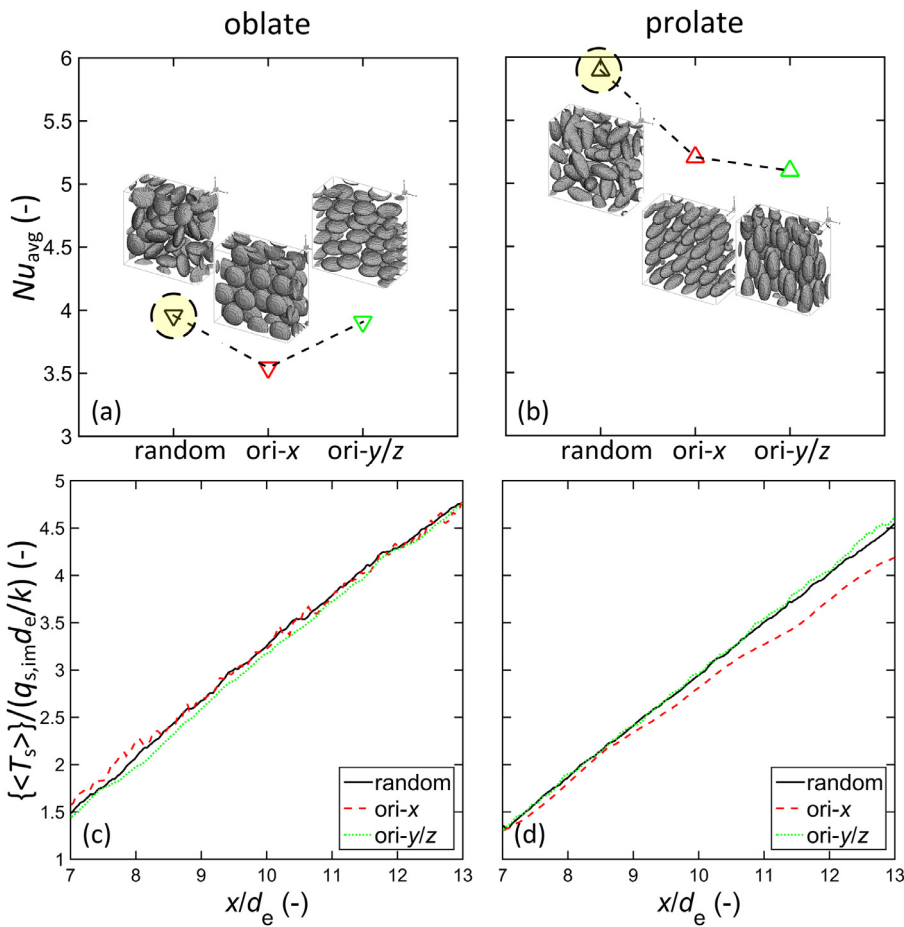


**Fig. 17.** Variation of  $Nu_{avg}$  versus specific orientations and axial temperature profile for  $Re=5$  at  $\varphi=0.3$ .

the  $y\text{/}z$ -direction. Along with the lowest  $Nu_{avg}$  in the  $x$ -direction, it implies that once there are oblate particles aligning their symmetry axis in the  $x$ -direction, large wake areas cause severe blocking which dominates mixing resulting in inefficient heat transfer compared to prolates.

## 6. Conclusion

By combining the DDF-IBM for velocity and the GC-IBM for temperature, a new DNS approach was proposed and employed

to study the heat transfer in fluid-particle flow with  $\varphi=0.1$  to 0.3 and  $Re=2.5$  to 200, confirming significant particle shape effect on  $Nu_{avg}$ . An isolated particle system has been used to validate the hydrodynamic part (DDF-IBM) and thermal part (GC-IBM), the results of which agree well with the literature. Moreover, the numerical convergence of heat transfer in the particle assemblies has been examined.

Generally, the computed  $Nu_{avg}$  agree well with the literature results. Correlations have been proposed for oblates and prolates by fitting the DNS data. At low  $\varphi$  (e.g.,  $=0.1$ ),  $Nu_{avg,prolate} > Nu_{avg,oblate}$

$> Nu_{avg,sphere}$ . However, at high  $\varphi$  (e.g., =0.3) and low  $Re$  (e.g., =5),  $Nu_{avg,prolate} > Nu_{avg,sphere} > Nu_{avg,oblate}$ . The study also suggests more uniform flow and hence better mixing may lead to higher  $Nu_{avg}$  for prolates, but oblates seem to have a more complex behavior attenuating and intensifying the heat transfer at low and high  $Re$  at high  $\varphi$ , respectively. Moreover, for additional cases with four specific orientation configurations, the relationship  $Nu_{avg,prolate} > Nu_{avg,oblate}$  still holds. A more convincing explanation and complementary studies, e.g., extending the range of particle aspect ratio and Prandtl number, are subject to future works, for which DNS will continue to be a powerful tool.

## Declaration of Competing Interest

None.

## CRediT authorship contribution statement

**Qi Chang:** Conceptualization, Data curation, Formal analysis, Investigation, Methodology, Software, Validation, Visualization, Writing - original draft, Writing - review & editing. **Liqiu Yang:** Investigation. **Wei Ge:** Funding acquisition, Investigation, Project administration, Supervision, Writing - original draft, Writing - review & editing.

## Acknowledgements

The authors gratefully acknowledge the financial support from the National Natural Science Foundation of China (Grand Nos. 21821005 and 91834303) and the Chinese Academy of Sciences (Grant Nos. QYZDJ-SSW-JSC029, XXH13506-301, and XDA21030700).

## References

- [1] D.J. Gunn, Transfer of heat or mass to particles in fixed and fluidised beds, *International Journal of Heat and Mass Transfer* 21 (4) (1978) 467–476.
- [2] H. Tavassoli, S.H.L. Kriebitzsch, M.A. Van der Hoef, E. Peters, J.A.M. Kuipers, Direct numerical simulation of particulate flow with heat transfer, *International Journal of Multiphase Flow* 57 (2013) 29–37.
- [3] S. Tenneti, B. Sun, R. Garg, S. Subramaniam, Role of fluid heating in dense gas–solid flow as revealed by particle-resolved direct numerical simulation, *International Journal of Heat and Mass Transfer* 58 (1–2) (2013) 471–479.
- [4] B. Sun, S. Tenneti, S. Subramaniam, Modeling average gas–solid heat transfer using particle-resolved direct numerical simulation, *International Journal of Heat and Mass Transfer* 86 (2015) 898–913.
- [5] B. Kravets, H. Krugel-Emden, Investigation of local heat transfer in random particle packings by a fully resolved LBM-approach, *Powder Technology* 318 (2017) 293–305.
- [6] Y. Chen, C.R. Müller, Lattice Boltzmann simulation of gas–solid heat transfer in random assemblies of spheres: The effect of solids volume fraction on the average Nusselt number for  $Re \leq 100$ , *Chemical Engineering Journal* 361 (2019) 1392–1399.
- [7] L. He, D.K. Tafti, Heat transfer in an assembly of ellipsoidal particles at low to moderate Reynolds numbers, *International Journal of Heat and Mass Transfer* 114 (2017) 324–336.
- [8] J. Lu, E.A.J.F. Peters, J.A.M. Kuipers, Direct numerical simulation of mass transfer in bidisperse arrays of spheres, *AIChE Journal* 66 (1) (2020) 1–17.
- [9] H. Tavassoli, E. Peters, J. Kuipers, Direct numerical simulation of non-isothermal flow through dense bidisperse random arrays of spheres, *Powder Technology* 314 (2017) 291–298.
- [10] L.W. Rong, Z.Y. Zhou, A.B. Yu, Lattice–Boltzmann simulation of fluid flow through packed beds of uniform ellipsoids, *Powder technology* 285 (2015) 146–156.
- [11] J. Gan, Z. Zhou, A. Yu, Particle scale study of heat transfer in packed and fluidized beds of ellipsoidal particles, *Chemical Engineering Science* 144 (2016) 201–215.
- [12] N. Kishore, S. Gu, Momentum and heat transfer phenomena of spheroid particles at moderate Reynolds and Prandtl numbers, *International Journal of Heat and Mass Transfer* 54 (11–12) (2011) 2595–2601.
- [13] C. Ke, S. Shu, H. Zhang, H. Yuan, D. Yang, On the drag coefficient and averaged Nusselt number of an ellipsoidal particle in a fluid, *Powder Technology* 325 (2018) 134–144.
- [14] A. Richter, P.A. Nikrityuk, Drag forces and heat transfer coefficients for spherical, cuboidal and ellipsoidal particles in cross flow at sub-critical Reynolds numbers, *International Journal of Heat and Mass Transfer* 55 (4) (2012) 1343–1354.
- [15] A. Richter, P.A. Nikrityuk, New correlations for heat and fluid flow past ellipsoidal and cubic particles at different angles of attack, *Powder technology* 249 (2013) 463–474.
- [16] C.W. Hirt, A.A. Amsden, J. Cook, An arbitrary Lagrangian-Eulerian computing method for all flow speeds, *Journal of computational physics* 14 (3) (1974) 227–253.
- [17] Q. Chang, W. Ge, Direct numerical simulation of wall-to-liquid heat transfer in turbulent particle-laden channel flow, *Chemical Engineering and Processing-Process Intensification* 157 (2020) 108023.
- [18] Q. Chang, S. Di, J. Xu, W. Ge, Direct numerical simulation of turbulent liquid-solid flow in a small-scale stirred tank, *Chemical Engineering Journal*, (2020) 127562.
- [19] R. Mittal, G. Iaccarino, Immersed boundary methods, *Annu. Rev. Fluid Mech* 37 (2005) 239–261.
- [20] M. Uhlmann, An immersed boundary method with direct forcing for the simulation of particulate flows, *Journal of Computational Physics* 209 (2) (2005) 448–476.
- [21] K. Nagendra, D.K. Tafti, K. Viswanath, A new approach for conjugate heat transfer problems using immersed boundary method for curvilinear grid based solvers, *Journal of Computational Physics* 267 (2014) 225–246.
- [22] W.-P. Breugem, A second-order accurate immersed boundary method for fully resolved simulations of particle-laden flows, *Journal of Computational Physics* 231 (13) (2012) 4469–4498.
- [23] T. Kempe, J. Fröhlich, An improved immersed boundary method with direct forcing for the simulation of particle laden flows, *Journal of Computational Physics* 231 (9) (2012) 3663–3684.
- [24] A.M. Roma, C.S. Peskin, M.J. Berger, An adaptive version of the immersed boundary method, *Journal of computational physics* 153 (2) (1999) 509–534.
- [25] K. Luo, J. Tan, Z. Wang, J. Fan, Particle-resolved direct numerical simulation of gas–solid dynamics in experimental fluidized beds, *AIChE Journal* 62 (6) (2016) 1917–1932.
- [26] Y. Tang, E. Peters, J.A.M. Kuipers, Direct numerical simulations of dynamic gas–solid suspensions, *AIChE Journal* 62 (6) (2016) 1958–1969.
- [27] S. Das, A. Panda, N.G. Deen, J.A.M. Kuipers, A sharp-interface Immersed Boundary Method to simulate convective and conjugate heat transfer through highly complex periodic porous structures, *Chemical Engineering Science* 191 (2018) 1–18.
- [28] C. Chatfield, Simple Method for Distance to Ellipse, in, <https://wet-robots.ghost.io/simple-method-for-distance-to-ellipse/>.
- [29] K. Luo, Z. Wang, J. Fan, K. Cen, Full-scale solutions to particle-laden flows: Multidirect forcing and immersed boundary method, *Physical Review E* 76 (6) (2007) 066709.
- [30] R.D. Falgout, U.M. Yang, in: *hypre: A library of high performance preconditioners*, Springer, 2002, pp. 632–641.
- [31] A. Xu, L. Shi, T. Zhao, Thermal effects on the sedimentation behavior of elliptical particles, *International Journal of Heat and Mass Transfer* 126 (2018) 753–764.
- [32] Sphere Point Picking, in, <https://mathworld.wolfram.com/SpherePointPicking.html>.
- [33] Uniform Random Orientation, in, <http://www.cognitive-antics.net/uniform-random-orientation/>.
- [34] G. Lu, J. Third, C. Müller, Discrete element models for non-spherical particle systems: From theoretical developments to applications, *Chemical Engineering Science* 127 (2015) 425–465.
- [35] D.J. Evans, S. Murad, Singularity free algorithm for molecular dynamics simulation of rigid polyatomics, *Molecular physics* 34 (2) (1977) 327–331.
- [36] S.K. Sanjeevi, J.T. Padding, Hydrodynamic forces on monodisperse assemblies of axisymmetric elongated particles: Orientation and voidage effects, *AIChE Journal* 66 (6) (2020) e16951.
- [37] S.K.P. Sanjeevi, J.A.M. Kuipers, J.T. Padding, Drag, lift and torque correlations for non-spherical particles from Stokes limit to high Reynolds numbers, *International Journal of Multiphase Flow* 106 (2018) 325–337.
- [38] J.M.D. valle, *Micrometrics*, Pitman Publishing, New York, 1948.
- [39] P. Bagchi, M. Ha, S. Balachandar, Direct numerical simulation of flow and heat transfer from a sphere in a uniform cross-flow, *J. Fluids Eng* 123 (2) (2001) 347–358.
- [40] W.E. Ranz, W.R. Marshall, Evaporation from drops, *Chem. eng. prog.* 48 (3) (1952) 141–146.
- [41] S. Whitaker, Forced convection heat transfer correlations for flow in pipes, past flat plates, single cylinders, single spheres, and for flow in packed beds and tube bundles, *AIChE Journal* 18 (2) (1972) 361–371.
- [42] Z.-G. Feng, E.E. Michaelides, Heat transfer in particulate flows with direct numerical simulation (DNS), *International Journal of Heat and Mass Transfer* 52 (3–4) (2009) 777–786.
- [43] A. Maheshwari, R.P. Chhabra, G. Biswas, Effect of blockage on drag and heat transfer from a single sphere and an in-line array of three spheres, *Powder technology* 168 (2) (2006) 74–83.
- [44] H. Tavassoli, Direct numerical simulation of dense gas–solid non-isothermal flows, *Eindhoven University* (2014).